

Bayesian constraints on covariant density functional equations of state of compact stars with new NICER mass-radius measurements

Jia-Jie Li^a, Yu Tian^a, Armen Sedrakian^{b,c}

^a*School of Physical Science and Technology, Southwest University, Chongqing 400715, China*

^b*Frankfurt Institute for Advanced Studies, D-60438 Frankfurt am Main, Germany*

^c*Institute of Theoretical Physics, University of Wrocław, 50-204 Wrocław, Poland*

Abstract

Recent advancements in astrophysical observations of compact stars, particularly the new and updated NICER constraints, have provided mass-radius (M - R) data for pulsars spanning masses from 1 to $2 M_{\odot}$. These data offer a unique opportunity to test modern theories of dense matter using multi-messenger constraints. Covariant density functional (CDF) models of nuclear matter, which capture a broad range of nuclear and astrophysical phenomena, provide a robust theoretical framework to interpret these observations. This study applies the Bayesian framework to a class of CDF models with density-dependent meson-nucleon couplings, specifically those based on nucleonic degrees of freedom. By incorporating the latest multi-messenger constraints, we impose tighter limits on the parameter space of these models and assess their consistency with observational data. Our analysis advances previous efforts by refining the density-dependence parameterization and integrating recent M - R ellipses. This enables more stringent evaluations of dense matter models in light of new astrophysical observations.

Keywords: Equation of state, Compact stars, Covariant density functional, Bayesian inference

1. Introduction

Recently, new NICER astrophysical constraints have been released for two pulsars — one canonical-mass $1.4 M_{\odot}$ star J0437-4715 (hereafter J0437, [1]), and the one-solar-mass star PSR J1231-1411 (J1231, [2]). Combining these with two previously reported data — the two-solar-mass pulsar PSR J0740+6620 (J0740, [3, 4]) and the canonical-mass star PSR J0030+0451 (hereafter J0030, [5, 6]), the mass range covered by the current data spans the range 1 to $2 M_{\odot}$. This data opens an unprecedented opportunity to explore models of modern theories of dense matter subject to astrophysical constraints. Notably, recent developments include the analysis of PSR J1231 which resulted in two different ellipses in the mass-radius (M - R) plane, depending on the radius prior [2] and the reanalysis of PSR J0030, which resulted in three different ellipses in the M - R plane, each corresponding to a different analysis method [7].

The covariant density functional (CDF) models of nuclear matter provide a rigorous framework to address the full range of available data on nuclear systems, ranging from the atomic chart to the astrophysics of compact stars (CSs), for reviews see [8–12]. These models were instrumental in addressing successfully such astrophysics problems as hyperon puzzle in conjunction with two-solar mass CSs and tidal deformability (TD) inference of GW170817 event. The CDF models are separated into broad classes which (a) have non-linear meson contributions to the effective Lagrangian and (b) keep only linear coupling but impose density-dependence of the coupling, which

captures the medium modifications of the meson-nucleon vertices, see reviews [10, 12] for discussions.

The Bayesian framework of constraining the properties of dense matter in CSs given the observational constraints — typically ellipses in the M - R diagram — has attracted recently significant attention. It allowed one to find correlations between the nuclear observables consistent with the astrophysical inferences. The Bayesian framework has been applied to models covering the range from fully physics agnostic non-parametric models [13–22] to microscopic models based on nuclear potentials [23–27] to density functional method-based CDF [28–36].

The aim of this paper is to apply the Bayesian framework to CDF models that have been developed in [37–41], all of which correspond to the class of models of CDF with linear meson-baryon couplings and density-dependent coupling constants. The utility of the CDF framework, when compared to agnostic models, lies in its ability to directly access the composition and quasiparticle spectra of constituents. These are essential for physical applications, such as studies of transport and neutrino interactions. Compared to microscopic models, CDFs enable efficient exploration of parameter spaces at reduced numerical cost. We aim to assess the compatibility of the parameter space over which these models are defined with the recent multi-messenger observations of CSs. Previous studies of this sort used simplified functions for density dependence of meson-baryon couplings [29, 32, 36]. Our analysis is aimed at revealing more stringent constraints on the CDF models given that the most recent astrophysical inferences have not been included in the Bayesian framework. Specifically, we will suggest and scrutinize different scenarios that incorporate different

Email addresses: jiajieli@swu.edu.cn (Jia-Jie Li), sedrakian@fias.uni-frankfurt.de (Armen Sedrakian)

combinations of the above-listed M - R ellipses. Previous studies employed simplified exponential density dependencies for the σ - and ω -meson fields, which are not aligned with the standard formulations typically used in these models. To address this inconsistency, the current work retains the established density-dependent CDF forms as previously applied in the literature.

The present study is limited to matter with nucleonic degrees of freedom, which eliminates the possibility of nucleation of heavy baryons (hyperons and Δ -resonances) [12, 40], as well as quark deconfinement [42, 43], at typically several times the nuclear saturation density. Such a restriction allows us to focus our analysis on a smaller set of parameters, which otherwise would contain the hyperonic couplings within our CDF approach, or parameters of quark matter equation of state (EOS) in any particular model of QCD. The impact of non-nucleonic degrees of freedom on CS observables has been extensively studied. For example, hyperonization reduces the maximum mass of CSs, therefore the correlations sensitive to the high density physics, such as those involving skewness of EOS will be affected [44, 45]. Furthermore, a non-monotonic speed of sound is obtained within such models. Although definitive proof is not yet available, several recent studies based on physics-agnostic treatments of high-density matter [18, 46, 47] suggest a decrease in the speed of sound once the non-nucleonic degrees of freedom nucleate. By construction, such behavior is not accounted for within the present CDF framework

2. CDF for nucleonic matter

We use the CDF approach based on the Lagrangian of stellar matter with nucleonic degrees of freedom $\mathcal{L} = \mathcal{L}_N + \mathcal{L}_m + \mathcal{L}_l$, where the nucleonic Lagrangian is given by

$$\mathcal{L}_N = \sum_N \bar{\psi}_N \left[\gamma^\mu (i\partial_\mu - g_\omega \omega_\mu - g_\rho \boldsymbol{\tau} \cdot \boldsymbol{\rho}_\mu) - (m_N - g_\sigma \sigma) \right] \psi_N, \quad (1)$$

where ψ_N are the nucleonic Dirac fields with mass m_N , σ , ω_μ , and $\boldsymbol{\rho}_\mu$ are the mesonic fields that mediate the interactions among the nucleon fields. The remaining pieces of the Lagrangian correspond to the mesonic and leptonic contributions, respectively.

The meson-nucleon couplings, which are density-dependent and are given by

$$g_m(\rho) = g_m(\rho_{\text{sat}}) f_m(r), \quad (2)$$

where index m refers to mesons, the coupling constant $g_m(\rho_{\text{sat}})$ is given at saturation density ρ_{sat} , and the function $f_m(r)$ depends on the ratio $r = \rho/\rho_{\text{sat}}$. For the isoscalar mesons

$$f_m(r) = a_m \frac{1 + b_m(r + d_m)^2}{1 + c_m(r + d_m)^2}, \quad m = \sigma, \omega, \quad (3)$$

with conditions $f_m(1) = 1$, $f_m''(0) = 0$, and $f_\sigma''(1) = f_\omega''(1)$, which reduce the number of free parameters. The density dependence for the isovector meson is taken in an exponential form:

$$f_\rho(r) = e^{-a_\rho(r-1)}. \quad (4)$$

Table 1: Symmetric nuclear matter (SNM) characteristics at saturation density [39] and pure neutron matter (PNM) properties from χ EFT computation [48] that constrain the CDF parameters. The prior distributions assumed for the quantities are either a Gaussian distribution (G) or a Uniform distribution (U).

	Quantity	Unit	Interval	Prior
SNM	ρ_{sat}	fm^{-3}	0.153 ± 0.005	G
	M_D^*	m_N	0.60 ± 0.05	G
	E_{sat}	MeV	-16.1 ± 0.2	G
	K_{sat}	MeV	230 ± 40	G
	Q_{sat}	MeV	$[-1000, 1500]$	U
	J_{sym}	MeV	32.5 ± 2.0	G
	L_{sym}	MeV	$[0, 100]$	U
PNM	$P(\rho)$	MeV/fm^3	N^3LO	G
	$\epsilon(\rho)$	MeV/fm^3	N^3LO	G

If we fix in the Lagrangian (1) the nucleon and meson masses to be (or close to) the ones in the vacuum then properties of infinite nuclear matter can be computed uniquely in terms of seven adjustable parameters. These are the three coupling constants at saturation density ($g_\sigma, g_\omega, g_\rho$), and four parameters ($a_\sigma, d_\sigma, d_\omega, a_\rho$) that control their density dependences. We consider uniform prior distributions of these seven CDF parameters within reasonable intervals.

3. Inference framework

The Bayesian analysis has been used in a variety of different research fields to infer the probability distribution of unknown parameters in a model by exploiting the information from observation. This is accomplished by relying on the Bayes' theorem,

$$p(\boldsymbol{\theta}|\mathbf{d}) = \frac{\mathcal{L}(\mathbf{d}|\boldsymbol{\theta}) p(\boldsymbol{\theta})}{\int \mathcal{L}(\mathbf{d}|\boldsymbol{\theta}) p(\boldsymbol{\theta}) d\boldsymbol{\theta}}, \quad (5)$$

where available knowledge on model parameters $\boldsymbol{\theta}$ is expressed as a prior distribution $p(\boldsymbol{\theta})$, by combining with observational data \mathbf{d} in terms of likelihood functions $\mathcal{L}(\mathbf{d}|\boldsymbol{\theta})$. The posterior distributions $p(\boldsymbol{\theta}|\mathbf{d})$ are then updated with the information from observables. The denominator is a normalization factor and acts as the evidence of data. Below, we present a brief discussion on the constraints and corresponding likelihoods we adopted in the present analysis.

3.1. Low-density nuclear matter properties

The energy density of isospin asymmetric matter is customarily split into an isoscalar and an isovector term:

$$E(\rho, \delta) \simeq E_0(\rho) + E_{\text{sym}}(\rho) \delta^2 + \mathcal{O}(\delta^4) \quad (6)$$

where $\rho = \rho_n + \rho_p$ is the baryonic density, with $\rho_{n(p)}$ denoting the neutron (proton) density, $\delta = (\rho_n - \rho_p)/\rho$ is the isospin asymmetry, and $E_0(\rho)$ and $E_{\text{sym}}(\rho)$ are, respectively, the energy of

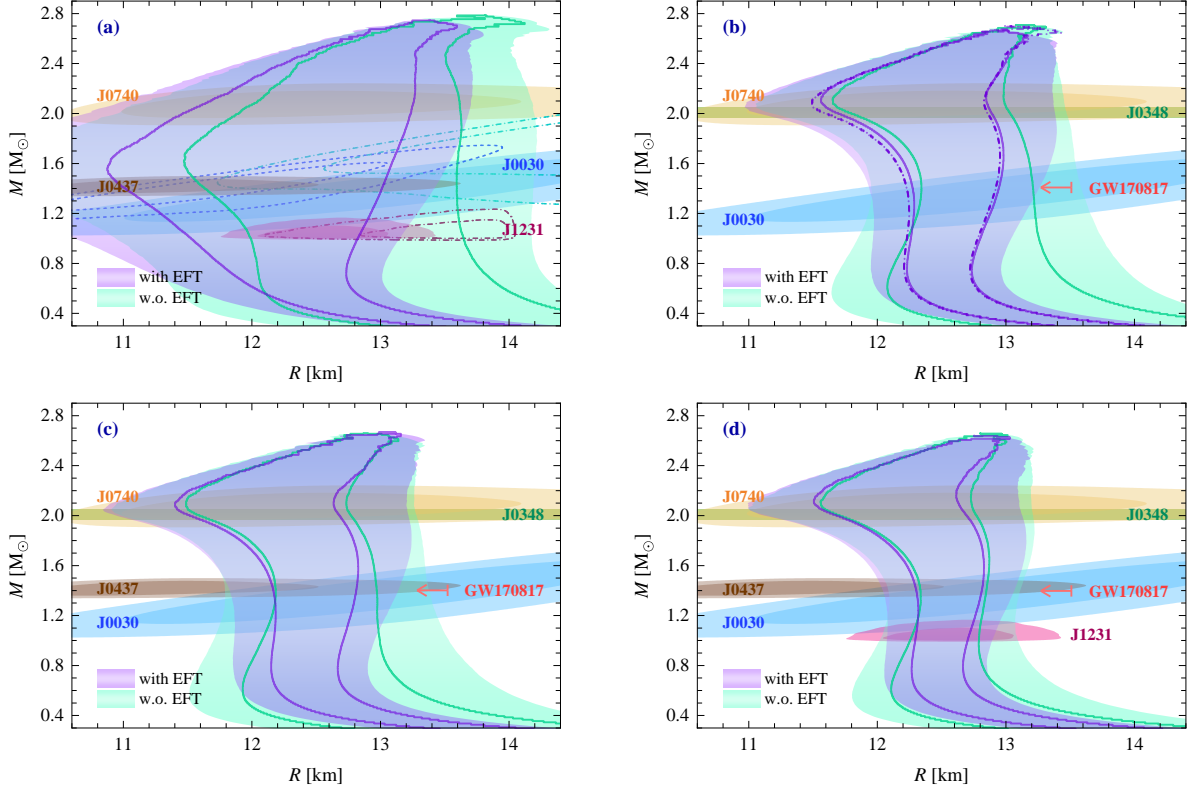


Figure 1: Posteriors for the mass-radius distribution under various constraints explored in this study are presented. The shaded regions represent the 95.4% credible intervals (CI), while the lines indicate the 68.3% CI. Panel (a) imposes constraints solely on low-density nucleonic matter, while panels (b), (c), and (d) incorporate additional astrophysical constraints. These include mass measurements from the massive pulsar J0348, tidal deformability constraints derived from the GW170817 and GW190425 events, and mass-radius estimates obtained from NICER observations. Specifically, panel (b) utilizes data from J0740 and J0030, panel (c) adds data from J0437 to this ensemble, and panel (d) further incorporates data from J1231. For comparison, the impact of the χ EFT constraint is highlighted in each panel. Panel (a) also provides an overview of new and updated NICER results, including the latest estimate for J0437 from [1], two estimates for J1231 from [2], the reanalysis of J0740 from [49], and three possible solutions for J0030 from [7]. Panel (b) includes results computed using previous NICER data from [3] and [5] for comparison.

symmetric matter and the symmetry energy. At densities close to the saturation ρ_{sat} Eq. (6) can be further Taylor expanded as

$$E(\rho, \delta) \simeq E_{\text{sat}} + \frac{1}{2!} K_{\text{sat}} \chi^2 + \frac{1}{3!} Q_{\text{sat}} \chi^3 + J_{\text{sym}} \delta^2 + L_{\text{sym}} \delta^2 \chi + \frac{1}{2!} K_{\text{sym}} \delta^2 \chi^2 + O(\chi^4, \chi^3 \delta^2), \quad (7)$$

where $\chi = (\rho - \rho_{\text{sat}})/3\rho_{\text{sat}}$. The coefficients of the expansion are known as *nuclear matter characteristics at saturation density*, namely, *incompressibility* K_{sat} , the *skewness* Q_{sat} , the *symmetry energy* J_{sym} and its *slope parameter* L_{sym} . The coefficients of the leading-order terms in the expansion, namely K_{sat} and J_{sym} are well determined, whereas the coefficients of higher-order terms, namely Q_{sat} and L_{sym} are not well known. In addition to the parameters in Eq. (7), the Dirac mass M_{D}^* at saturation is well-constrained. This parameter plays a crucial role in the quantitative description of finite nuclei phenomena, such as spin-orbit splitting. For quantities known with an uncertainty of approximately 10%, we adopt Gaussian priors, while for others, we use uniform priors. The mean values, standard deviations, or intervals for each parameter are detailed in Table 1. Notably, broader ranges are considered for Q_{sat} and L_{sym} to encompass the variations reported in different studies.

In addition to the constraints above, we incorporate results for pure neutron matter up to around nuclear saturation density based on chiral effective field theory (χ EFT) interactions. These constrain the low-density regime of nucleonic EOS. In the present multi-messenger analyses, we use the N^3LO constraints from [48] and assume the uncertainty band as a Gaussian distribution. As an illustration of the impact of this constraint, we show in Fig. 1 (a) the M - R posterior distributions at 68.3% and 95.4% CIs for models considering only low-density nucleonic matter constraints.

3.2. Astrophysical observations

We now briefly describe our implementations of the likelihoods for various astrophysical observations. The product of the individual likelihoods of these sources finally gives the total likelihood.

- The *NICER* collaborations have delivered the joint measurement of mass and radius through pulse profile modeling of four millisecond pulsar: a massive $\sim 2 M_{\odot}$ star PSR J0740, two canonical-mass $\sim 1.4 M_{\odot}$ stars PSR J0030 and J0437, and a low mass $\sim 1 M_{\odot}$ star PSR J1231. We construct the likelihood function for each of the sources using the Gaussian kernel density estimation (KDE) with

Table 2: New astrophysical constraints are used for the scenarios in the present work.

Scenario	J0348	GW ^a (2)	J0740 ST-U	J0437 CST+PDT	J0030 ^b		J1231 ^c	
					ST+PST	ST+PDT	PDT-U	PDT-U (i) PDT-U (ii)
Baseline	×	×	×		×			
A	×	×	×	×	×			×
B	×	×	×	×		×		×
C	×	×	×	×			×	×
D	×	×	×	×	×			
E	×	×	×	×		×		×
F	×	×	×	×			×	×

^a Both the confirmed two (most likely) binary neutron star mergers GW170817 [50] and GW190425 [51] are considered.

^b For PSR J0030, the ST+PST refers to the NICER-only analysis of the same data set from [5] with an improved analysis pipeline and setting, ST+PDT and PDT-U are two modes preferred in the joint analysis of NICER and XMM data for which the ST+PDT results are more consistent with the magnetic field geometry inferred for the gamma-ray emission for this source, and the PDT-U is the most complex model and is preferred by the Bayesian evidence [7].

^c For PSR J1231, the PDT-U (i) refers to the model that used an informative radius prior based on the results of [52], and (ii) the one that limited the radius between 10 and 14 km.

the released posterior (M, R) samples \mathcal{S} ,

$$\mathcal{L}_{\text{NICER}}(\theta_{\text{EOS}}) = \text{KDE}(M, R | \mathcal{S}), \quad (8)$$

where the mass M and radius R for the star are functions of its central pressure and the sampled EOS parameters θ_{EOS} . The model samples of each pulsar we implement for the present analysis are listed in Table 2.

- To date, the *gravitational wave* (GW) events GW170817 [50] and GW190425 [51] are the only confirmed binary neutron star mergers detected during the LVK collaboration’s observing runs. In the analysis of a single GW event, the likelihood function used for Bayesian inference depends on a parameter vector, θ_{GW} , which includes two key components: parameters relevant for constraining the EOS of dense matter, θ_{EOS} , and nuisance parameters, $\theta_{\text{nuis.}}$, necessary for modeling GW-emitting binaries. However, the inclusion of numerous nuisance parameters — often numbering in the dozens — substantially slows down the sampling process. To address this, the likelihood is computed using high-precision interpolation in TOAST [53], which marginalizes over these nuisance parameters to streamline the analysis. It can be written

$$\mathcal{L}_{\text{GW}}(\theta_{\text{EOS}}) = F(\mathcal{M}, q, \Lambda_1, \Lambda_2), \quad (9)$$

where $\mathcal{M} = (M_1 M_2)^{3/5} / (M_1 + M_2)^{1/5}$ is the chirp mass, $q = M_1 / M_2$ is the mass ratio, and $\Lambda_1(M_1)$ and $\Lambda_2(M_2)$ the TDs of the individual star.

- To approximate the mass measurements of *massive pulsars* (MP), e.g., PSR J0348+0432 (hereafter J0348, [54]), we use Gaussian distributions, and the cumulative density function of Gaussian is applied to build the likelihood,

$$\mathcal{L}_{\text{MP}}(\theta_{\text{EOS}}) = \frac{1}{2} \left[1 + \text{erf} \left(\frac{M_{\text{max}}(\theta_{\text{EOS}}) - M}{\sqrt{2}\sigma} \right) \right], \quad (10)$$

where $\text{erf}(x)$ is the error function, M and σ are the mean and the standard deviation of the mass measurements for

the source, respectively. We do not take into account the mass measurement for PSR J0740 [55, 56], to avoid double counting with its NICER estimate.

4. Results and implications

Our results are summarized in Figs. 1–4. We apply the astrophysical and theoretical constraints both selectively and in concert to elucidate the importance of their individual impact as well as the overall picture that emerges from a combination of such constraints. We first discuss the roles of constraints individually.

4.1. Impact of chiral EFT constraint

Among the families of CDF parameterization of neutron matter of the EOS of dense matter, only those are compatible with the χ EFT which are soft at low densities and remain such up to $2\text{--}3\rho_{\text{sat}}$. More quantitatively, the CDFs that are compatible with χ EFT have the range of symmetry energy and its slope at nuclear saturation density limited by $29.5 \leq J_{\text{sym}} \leq 33$ MeV and $35 \leq L_{\text{sym}} \leq 60$ MeV (at 95.4% CI), respectively [40]. This leads to small uncertainty bands for radii of sub-canonical-mass stars, as illustrated in Fig. 1. As these constraints apply only at low density, it is evident that the density dependence of isovector quantities J_{sym} and L_{sym} have little impact on the properties of high-mass CSs. This is clearly seen in panels (b–d) of Fig. 1 where the posterior distributions for computations with and without χ EFT constraint are almost identical for sequences with $M > 1.4 M_{\odot}$.

4.2. Impact of individual astrophysical source

The masses of massive pulsars PSR J0348 and J0740 place strict constraints on the high-density behavior of nucleonic EOS — characterized by the value of Q_{sat} in a CDF model — which is set to $Q_{\text{sat}} \gtrsim -700$ MeV. For lower values of this parameter, the masses of these pulsars are not reproduced. Furthermore, they impact the lower value of the radius of stars, which is clearly visible by comparing panels (a) and (b) in Fig. 1. Including these objects results in the lower limit of the radius of a $2 M_{\odot}$

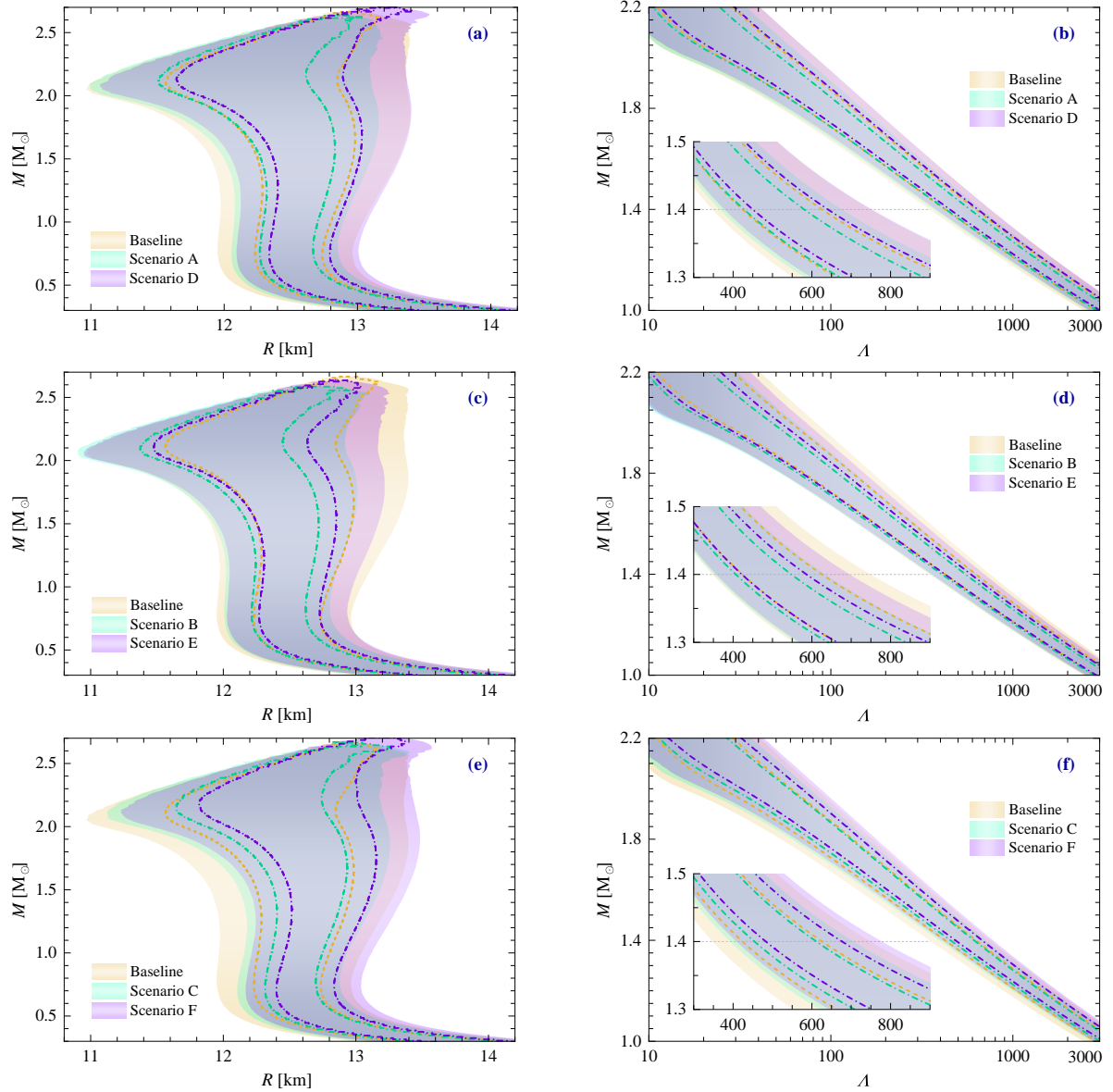


Figure 2: Posteriors for mass-radius (left panels) and mass-tidal deformability (right panels) distributions under seven scenarios explored in this work. The shaded regions represent the distributions at 95.4% CI, while the lines for results at 68.3% CI. In the right panels, the insets magnify the TDs for typical compact stars.

star ~ 11 km at 95.4% CI. Combining with the lower limit on the value of L_{sym} (constrained by χEFT) one finds for the radius of a canonical-mass ($1.4 M_{\odot}$) star $R_{1.4} \gtrsim 12$ km. On the other hand, the ellipses for PSR J0348 and J0740 do not limit the radii from above significantly. More stringent constraint on this limit comes from TDs derived from GW170817 event, which place an *upper limit* on the radii of canonical-mass stars $R_{1.4} \lesssim 13.5$ km. Furthermore, we have checked the posteriors by replacing the updated NICER estimates with previous data from [3] and [5], the difference for boundaries is well within 0.1 km. This further strengthens the importance of maximum mass and GW constraints for dense matter modeling.

In Fig. 1 (c), the M - R ellipse derived for PSR J0437 significantly overlaps with the M - R inferences from GW170817 event [51], which reinforces the selection of EOS based solely

on GW data or PSR J0437 data. Indeed, as shown in Fig. 1 (b, c), inclusion of PSR J0437 inference in addition to GW data shifts the M - R distributions towards a lower radius but only by ~ 0.2 km.

Once the M - R estimate from the PDT-U (i) model for PSR J1231 is included, the posterior region is narrowed noticeably by 0.2 km from both sides; see Fig. 1 (d). This narrowing is because the J1231 PDT-U (i) results are consistent with the inferred radius of J0437. However, if the estimate from the PDT-U (ii) model which favors a larger radius is included in the analysis, the upper limit for radius is relaxed by about 0.3 km; see Fig. 2 (a).

In closing, the mass measurements of PSR J0348 and J0740, along with the TDs inferred from GW170817 and the χEFT calculations, provide fundamental constraints for determining

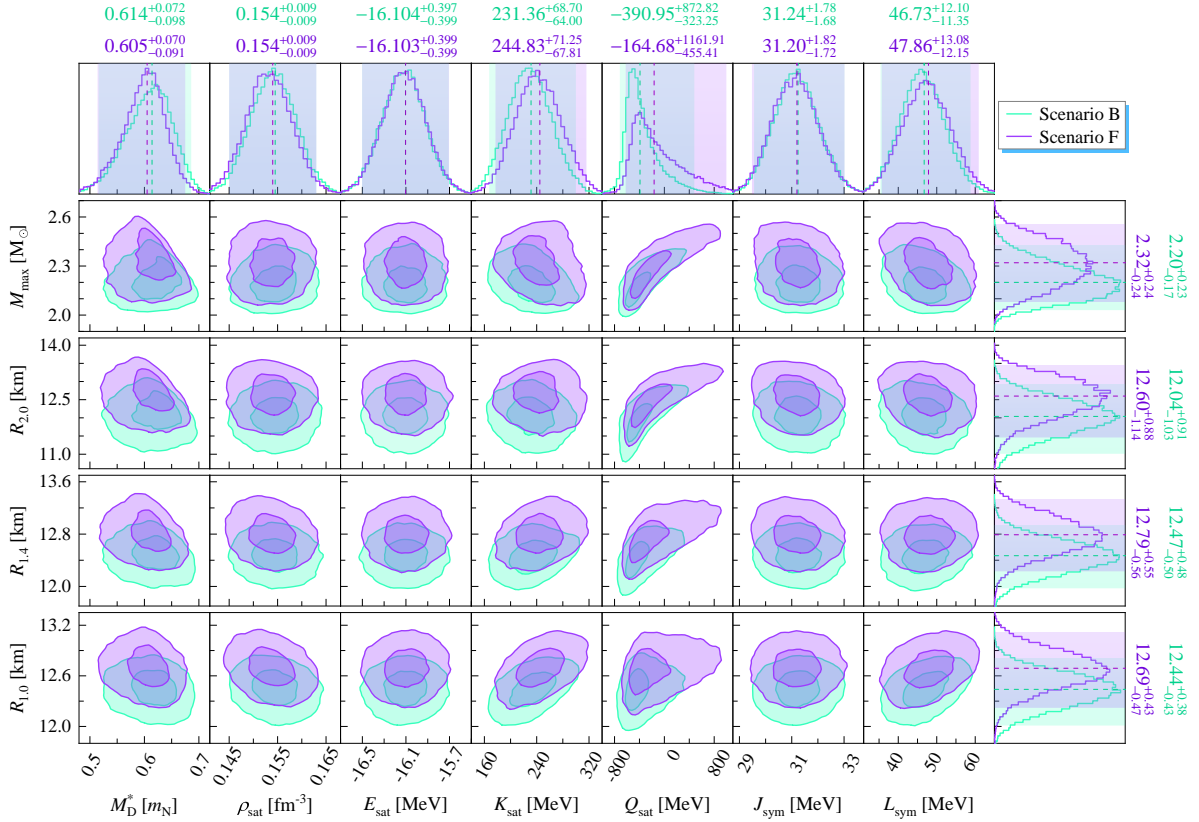


Figure 3: Posteriors for the correlations of characteristic parameters of symmetric nuclear matter at saturation and gross properties of compact stars under scenarios B and F which allow for the softest and stiffest models respectively. The light and dark shaded regions indicate respectively the 68.3% and 95.4% CI regions of the two-dimensional distributions. The one-dimensional posteriors for each quantity are given along the plots where vertical lines indicate the median positions and shaded intervals for -95.4% CI, respectively.

the basic posterior region of the M - R distribution. This posterior region shows significant overlap with the NICER estimates for pulsars. Consequently, we designate the posterior shown in Fig. 1 (b) as the “Baseline” for comparison with the full posteriors presented in Fig. 2, which incorporate NICER estimates for all four pulsars.

4.3. Implications from multimessenger data

Fig. 2 summarizes the posteriors for M - R and M - Λ distributions under seven different scenarios A - F and “Baseline” defined in Table 2. Overall the posterior distributions for M - R feature similar shapes. The posterior distributions narrow somewhat compared to the “Baseline” scenario, due to the combined effect of the PSR J0030 and J0437 NICER results, but most of the scenarios fully remain within the “Baseline” contours (with the exception of scenario F). The posterior distributions for TD naturally show similar trends as for the M - R posteriors.

As anticipated, the new NICER estimates for PSR J0437 and J1231, along with the reanalysis of PSR J0030, affect only the finer details of the posterior compared to the “Baseline” scenario. The tightest credible regions arise in scenario B, where more compact estimates for PSR J1231 (PDT-U (i) model) and J0030 (ST+PDT model), favoring softer EOS at densities below 2 and $3\rho_{\text{sat}}$, respectively, are used; see Fig. 2 (b, c). In contrast, the widest credible regions are predicted in the scenario

F, which incorporates less compact estimates for PSR J1231 (PDT-U (ii) model) and J0030 (PDT-U model); see Fig. 2 (d, e).

Fig. 3 illustrates the posterior distributions for the correlations between the characteristic parameters of nuclear matter at saturation density and the macroscopic properties of CSs under scenarios B and F. The characteristic parameters generally follow Gaussian distributions, except for the isoscalar skewness, Q_{sat} . The correlations between these parameters and the properties of CSs are similar across both scenarios. The isoscalar skewness, Q_{sat} , which influences both the maximum masses and radii of CSs, plays a dominant role in determining the maximum mass by effectively modifying the EOS at supra-saturation densities. Meanwhile, the isovector slope, L_{sym} , constrained by χ EFT calculations of low-density neutron matter, is narrowly distributed around $L_{\text{sym}} \sim 47$ MeV and has negligible impact on the overall properties of massive CSs.

Scenario B favors softer EOS featuring lower values for the incompressibility, $K_{\text{sat}} = 231.4^{+34.4}_{-33.3}$ MeV and negative values for the skewness, $Q_{\text{sat}} = -391.0^{+333.6}_{-170.2}$ MeV (at 68.3% CI); while scenario F favors stiffer EOS featuring higher values for $K_{\text{sat}} = 244.8^{+36.4}_{-34.7}$ MeV and allows for positive value for $Q_{\text{sat}} = -164.7^{+548.9}_{-280.1}$ MeV (at 68.3% CI). The value of Q_{sat} can further reach up to 900 MeV at a 95.4% CI. Note that in our modeling, the parameters K_{sat} and Q_{sat} are independent of each other,

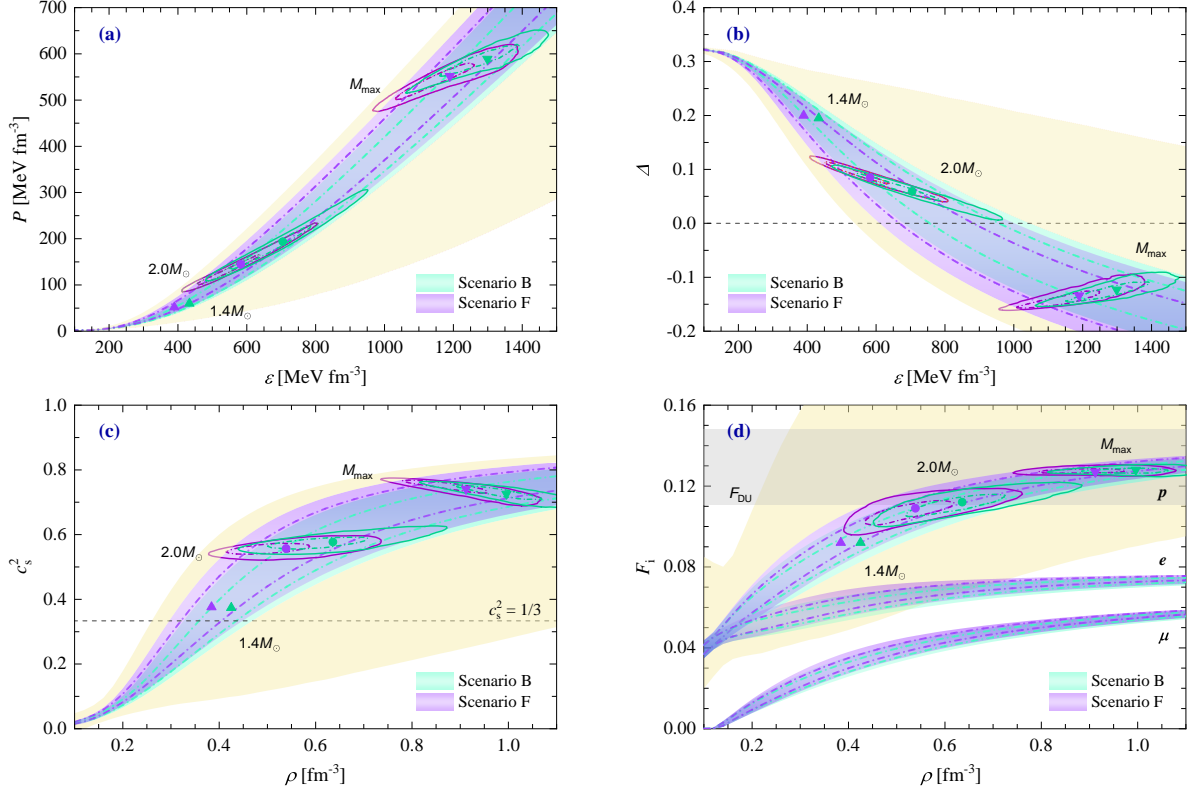


Figure 4: Posteriors for the nucleonic equation of state (panel a) distribution and dimensionless quantities characterizing the properties of dense matter – trace anomaly Δ (panel b), sound speed squared c_s^2 (panel c), and the particle fraction (panel d) under scenarios B and F which allow for the softest and stiffest models respectively. The shaded regions represent the distributions at 95.4% CI, while the lines for 68.3% CI. In each panel, the contours show the corresponding posterior distributions and symbols of the median positions of the respective 1.4 , $2.0 M_\odot$ stars and the maximum-mass configurations. In panel (d) the gray band labeled with F_{DU} frames the possible threshold values for the onset of direct Urca (DU) cooling process. The 99.7% CI regions after applying only the SNM constraints at saturation density are incorporated as well (in light yellow).

this is in contrast to previous studies of this type which simplified the functions (3) for density dependence of meson-baryon couplings [29, 32, 36].

Thus, scenarios B and F represent two distinct combinations of the current NICER estimates for pulsars, corresponding to the softest and stiffest models, respectively. The radius for a canonical-mass star is $R_{1.4} = 12.47^{+0.48}_{-0.50}$ km (at 95.4% CI) for scenario B and $12.79^{+0.55}_{-0.56}$ km for scenario F. The corresponding TD is $\Lambda_{1.4} = 472^{+163}_{-121}$ for scenario B and 571^{+207}_{-162} (at 95.4% CI) for scenario F. The maximum mass is $M_{\text{max}} = 2.20^{+0.23}_{-0.17} M_\odot$ and $2.32^{+0.24}_{-0.24} M_\odot$ respectively for scenarios B and F. The latter scenario therefore allows for a static CS interpretation for the secondary component of the GW190814 event [57].

Fig. 4 shows the posterior for EOS distribution and dimensionless quantities characterizing the properties of dense strongly interacting matter – the dimensionless trace anomaly $\Delta = 1/3 - P/\epsilon$ [58] (panel b), sound speed squared c_s^2 (panel c) – and the particle fraction (panel d) under scenarios B and F, respectively. For each scenario, the median positions of the respective 1.4 , $2.0 M_\odot$ and the maximum-mass configurations are marked in the plots.

In Fig. 4 (b), the trace anomaly Δ in the innermost cores of massive CSs ($M \gtrsim 2.0 M_\odot$) tends to approach zero and takes negative values for maximum mass configurations. The lower

limits are predicted as $\Delta \geq -0.123^{+0.038}_{-0.027}$ (at 95.4% CI) for scenario B and $\Delta \geq -0.134^{+0.049}_{-0.023}$ for scenario F. These results align with the constraints reported in [59], which are derived using agnostic EOS models.

Fig. 4 (c) shows the ranges of sound speed squared c_s^2 predicted by the EOS models, which is directly related to the slope of the EOS. Observations of two-solar mass CSs suggest that the pressure must rise rapidly with increasing energy density to counteract gravitational collapse. On the other hand, it is well known that the so-called conformal limit $c_s^2 = 1/3$ (in units of speed of light) must be reached at extremely high densities, where interactions between ultra-relativistic quarks vanish due to asymptotic freedom. Our results agree with the studies which indicate that the bound $c_s^2 \leq 1/3$ is significantly violated (see e.g., [45, 60–63]). At the same time, it shows that the CDF models are capable of producing massive CSs without violating the causality, i.e., $c_s^2 > 1$ which is not the case for (some) non-relativistic approaches. Note also, that the slope of the c_s remains convex above saturation density, which is in contrast to the case of hypernuclear matter treated in mean-field approximation, in which case the slope becomes concave at the point of onset of heavy baryons [44, 45]. It also contrasts the case where phase transition is allowed at densities relevant for CSs which could lead to a decrease in the speed of sound before reaching

its asymptotically free value [64].

In Fig. 4 (d) the gray band indicates the direct Urca (DU) threshold, which is, however, model dependent [65]. For μ^- free case the threshold value is 11.1%; in the limit of massless muons, which is applicable for high densities matter, it yields an upper limit of 14.8%. As seen in this plot, due to the softness of the nucleonic EOS at low densities, the DU process will be mostly disallowed in CSs with $M \leq 2 M_\odot$ utilizing CDF EOS. However, note that the DU threshold may be smoothed out due to short-range correlations in dense matter [66].

5. Conclusions

Our analysis demonstrates that Bayesian inference applied to CDF models with density-dependent couplings successfully reconciles recent astrophysical observations with theoretical predictions for dense nuclear matter. The M - R and M - Λ distributions derived under various observational scenarios reveal that maximum mass measurements, tidal deformability constraints from GW events, and low-density properties constrained by χ EFT play crucial roles in determining the EOS for CSs. Notably, the softer EOS models, favored under scenario B, predict lower radii and TDs for canonical-mass stars compared to the stiffer EOS models favored under scenario F, while remaining consistent with NICER and multimessenger data. This balance of constraints illustrates the robustness of CDF models in addressing the diverse observational data for CSs.

Importantly, the inclusion of updated NICER constraints for pulsars such as PSR J0437 and J1231 refines the posterior distributions, narrowing the credible regions of EOS parameters, particularly for sub-canonical and canonical-mass stars. The results highlight that the stiffness of the EOS at high densities, driven by isoscalar skewness Q_{sat} , governs the maximum masses and TDs of massive CSs, with implications for interpreting GW190814's secondary component as a static CS. Overall, this work provides tighter constraints on the EOS, advancing our understanding of dense nuclear matter and its behavior under extreme conditions. The approach underscores the importance of combining multimessenger observations and advanced theoretical frameworks to enhance the fidelity of nuclear astrophysics models.

Acknowledgments

J.L. and Y.T. acknowledge the support of the National Natural Science Foundation of China under Grant No. 12105232 and No. 12475150. A. S. is funded by Deutsche Forschungsgemeinschaft Grant No. SE 1836/6-1 and the Polish NCN Grant No. 2023/51/B/ST9/02798.

Declaration of competing interest

The authors declare that they have no known competing financial interests or personal relationships that could have appeared to influence the work reported in this paper.

Data availability

Data will be made available on request.

Appendix:

Key quantities of compact stars and nuclear matter, and the parameters for underlying CDFs

In this appendix, we present the characteristic parameters of symmetric nuclear matter at saturation density and key gross quantities of CSs predicted by CDFs under seven different scenarios in Tables 3 and 4, respectively. The parameter values for underlying CDFs are given in Table 5. In Table 3 we also show those values for higher order parameters Z_{sat} for isoscalar sector and K_{sym} , Q_{sym} and Z_{sym} for isovector sector which are not allowed to vary freely and thus are the predictions of CDFs, once if the low-order characteristics are determined.

References

- [1] D. Choudhury, T. Salmi, S. Vinciguerra, et al., A NICER View of the Nearest and Brightest Millisecond Pulsar: PSR J0437–4715, *Astrophys. J. Lett.* 971 (2024) L20. [arXiv:2407.06789](#), [doi:10.3847/2041-8213/ad5a6f](#).
- [2] T. Salmi, J. S. Deneva, P. S. Ray, et al., A NICER View of PSR J1231–1411: A Complex Case, *Astrophys. J.* 976 (2024) 58. [arXiv:2409.14923](#), [doi:10.3847/1538-4357/ad81d2](#).
- [3] T. E. Riley, A. L. Watts, P. S. Ray, et al., A NICER View of the Massive Pulsar PSR J0740+6620 Informed by Radio Timing and XMM-Newton Spectroscopy, *Astrophys. J. Lett.* 918 (2021) L27. [arXiv:2105.06980](#), [doi:10.3847/2041-8213/ac0a81](#).
- [4] M. C. Miller, F. K. Lamb, A. J. Dittmann, et al., The Radius of PSR J0740+6620 from NICER and XMM-Newton Data, *Astrophys. J. Lett.* 918 (2021) L28. [arXiv:2105.06979](#), [doi:10.3847/2041-8213/ac089b](#).
- [5] T. E. Riley, A. L. Watts, S. Bogdanov, et al., A NICER View of PSR J0030+0451: Millisecond Pulsar Parameter Estimation, *Astrophys. J. Lett.* 887 (2019) L21. [arXiv:1912.05702](#), [doi:10.3847/2041-8213/ab481c](#).
- [6] M. C. Miller, F. K. Lamb, A. J. Dittmann, et al., PSR J0030+0451 Mass and Radius from NICER Data and Implications for the Properties of Neutron Star Matter, *Astrophys. J. Lett.* 887 (2019) L24. [arXiv:1912.05705](#), [doi:10.3847/2041-8213/ab50c5](#).
- [7] S. Vinciguerra, T. Salmi, A. L. Watts, et al., An Updated Mass–Radius Analysis of the 2017–2018 NICER Data Set of PSR J0030+0451, *Astrophys. J.* 961 (2024) 62. [arXiv:2308.09469](#), [doi:10.3847/1538-4357/acfb83](#).
- [8] D. Vretenar, A. V. Afanasjev, G. A. Lalazissis, P. Ring, Relativistic Hartree Bogoliubov theory: static and dynamic aspects of exotic nuclear structure, *Phys. Rept.* 409 (2005) 101–259. [doi:10.1016/j.physrep.2004.10.001](#).
- [9] T. Niksic, D. Vretenar, P. Ring, Relativistic Nuclear Energy Density Functionals: Mean-Field and Beyond, *Prog. Part. Nucl. Phys.* 66 (2011) 519–548. [arXiv:1102.4193](#), [doi:10.1016/j.ppnp.2011.01.055](#).
- [10] M. Oertel, M. Hempel, T. Klähn, S. Typel, Equations of state for supernovae and compact stars, *Rev. Mod. Phys.* 89 (2017) 015007. [arXiv:1610.03361](#), [doi:10.1103/RevModPhys.89.015007](#).
- [11] J. Yang, J. Piekarewicz, Covariant Density Functional Theory in Nuclear Physics and Astrophysics, *Ann. Rev. Nucl. Part. Sci.* 70 (2020) 21–41. [arXiv:1912.11112](#), [doi:10.1146/annurev-nucl-101918-023608](#).
- [12] A. Sedrakian, J.-J. Li, F. Weber, Heavy baryons in compact stars, *Prog. Part. Nucl. Phys.* 131 (2023) 104041. [arXiv:2212.01086](#), [doi:10.1016/j.ppnp.2023.104041](#).

Table 3: Characteristic parameters of symmetric nuclear matter at saturation density from the posterior distributions for the different astrophysical scenarios. The upper and lower values correspond to the 68.3% CI.

Par.	Unit	Baseline	Scenario A	Scenario B	Scenario C	Scenario D	Scenario E	Scenario F
M_D^*	m_N	$0.609^{+0.038}_{-0.044}$	$0.611^{+0.038}_{-0.045}$	$0.614^{+0.039}_{-0.047}$	$0.608^{+0.037}_{-0.044}$	$0.607^{+0.038}_{-0.045}$	$0.611^{+0.039}_{-0.046}$	$0.605^{+0.035}_{-0.043}$
ρ_{sat}	fm^{-3}	$0.154^{+0.005}_{-0.005}$	$0.154^{+0.005}_{-0.005}$	$0.154^{+0.005}_{-0.005}$	$0.154^{+0.005}_{-0.005}$	$0.154^{+0.005}_{-0.005}$	$0.154^{+0.005}_{-0.005}$	$0.154^{+0.005}_{-0.005}$
E_{sat}	MeV	$-16.11^{+0.20}_{-0.20}$	$-16.11^{+0.20}_{-0.20}$	$-16.10^{+0.20}_{-0.20}$	$-16.11^{+0.20}_{-0.20}$	$-16.11^{+0.20}_{-0.20}$	$-16.11^{+0.20}_{-0.20}$	$-16.10^{+0.20}_{-0.20}$
K_{sat}	MeV	$233.9^{+37.1}_{-35.5}$	$234.1^{+35.4}_{-33.3}$	$231.4^{+34.4}_{-33.3}$	$235.2^{+35.0}_{-33.3}$	$242.8^{+36.1}_{-35.8}$	$239.1^{+36.3}_{-35.5}$	$244.8^{+36.4}_{-34.7}$
Q_{sat}	MeV	$-278.4^{+499.2}_{-237.7}$	$-330.6^{+409.5}_{-200.2}$	$-391.0^{+333.6}_{-170.2}$	$-249.8^{+469.7}_{-238.7}$	$-271.7^{+493.4}_{-228.7}$	$-357.4^{+376.1}_{-182.8}$	$-164.7^{+548.9}_{-280.1}$
Z_{sat}	MeV	4961^{+1630}_{-2296}	4888^{+1574}_{-2340}	4931^{+1595}_{-2330}	4932^{+1544}_{-2289}	4626^{+1714}_{-2472}	4652^{+1718}_{-2529}	4641^{+1663}_{-2508}
J_{sym}	MeV	$31.18^{+0.88}_{-0.86}$	$31.23^{+0.88}_{-0.86}$	$31.24^{+0.88}_{-0.86}$	$31.18^{+0.89}_{-0.85}$	$31.22^{+0.90}_{-0.85}$	$31.27^{+0.88}_{-0.85}$	$31.20^{+0.89}_{-0.88}$
L_{sym}	MeV	$46.47^{+6.33}_{-5.98}$	$46.92^{+5.93}_{-5.82}$	$46.73^{+5.94}_{-5.67}$	$46.73^{+6.04}_{-5.95}$	$47.80^{+6.30}_{-6.05}$	$47.78^{+6.07}_{-5.97}$	$47.86^{+6.46}_{-6.27}$
K_{sym}	MeV	$-99.3^{+25.6}_{-17.3}$	$-102.6^{+23.2}_{-15.8}$	$-106.0^{+21.0}_{-14.7}$	$-98.3^{+25.1}_{-16.9}$	$-99.3^{+24.8}_{-16.9}$	$-104.5^{+21.6}_{-14.9}$	$-94.2^{+26.6}_{-18.2}$
Q_{sym}	MeV	$797.1^{+156.9}_{-173.5}$	$778.9^{+159.1}_{-163.1}$	$776.1^{+155.5}_{-159.1}$	$792.1^{+158.2}_{-166.3}$	$757.8^{+165.5}_{-175.1}$	$751.2^{+162.7}_{-166.1}$	$765.3^{+166.5}_{-177.0}$
Z_{sym}	MeV	-5616^{+1696}_{-2312}	-5276^{+1560}_{-2202}	-5079^{+1435}_{-1988}	-5618^{+1695}_{-2395}	-5330^{+1649}_{-2401}	-5011^{+1487}_{-2080}	-5686^{+1820}_{-2596}

- [13] G. Raaijmakers, T. E. Riley, A. L. Watts, et al., A *NICER* view of PSR J0030+0451: Implications for the dense matter equation of state, *Astrophys. J. Lett.* 887 (2019) L22. [arXiv:1912.05703](#), [doi:10.3847/2041-8213/ab451a](#).
- [14] P. Landry, R. Essick, K. Chatzioannou, Nonparametric constraints on neutron star matter with existing and upcoming gravitational wave and pulsar observations, *Phys. Rev. D* 101 (2020) 123007. [arXiv:2003.04880](#), [doi:10.1103/PhysRevD.101.123007](#).
- [15] G. Raaijmakers, S. K. Greif, T. E. Riley, et al., Constraining the dense matter equation of state with joint analysis of *NICER* and *LIGO/Virgo* measurements, *Astrophys. J. Lett.* 893 (2020) L21. [arXiv:1912.11031](#), [doi:10.3847/2041-8213/ab822f](#).
- [16] I. Legred, K. Chatzioannou, R. Essick, S. Han, P. Landry, Impact of the PSR J0740+6620 radius constraint on the properties of high-density matter, *Phys. Rev. D* 104 (2021) 063003. [arXiv:2106.05313](#), [doi:10.1103/PhysRevD.104.063003](#).
- [17] P. T. H. Pang, I. Tews, M. W. Coughlin, M. Bulla, C. Van Den Broeck, T. Dietrich, Nuclear Physics Multimessenger Astrophysics Constraints on the Neutron Star Equation of State: Adding *NICER*'s PSR J0740+6620 Measurement, *Astrophys. J.* 922 (2021) 14. [arXiv:2105.08688](#), [doi:10.3847/1538-4357/ac19ab](#).
- [18] S. Altiparmak, C. Ecker, L. Rezzolla, On the Sound Speed in Neutron Stars, *Astrophys. J. Lett.* 939 (2) (2022) L34. [arXiv:2203.14974](#), [doi:10.3847/2041-8213/ac9b2a](#).
- [19] E. Annala, T. Gorda, E. Katerini, A. Kurkela, J. Nättilä, V. Paschalidis, A. Vuorinen, Multimessenger Constraints for Ultradense Matter, *Phys. Rev. X* 12 (2022) 011058. [arXiv:2105.05132](#), [doi:10.1103/PhysRevX.12.011058](#).
- [20] E. Annala, T. Gorda, J. Hirvonen, O. Komoltsev, A. Kurkela, J. Nättilä, A. Vuorinen, Strongly interacting matter exhibits deconfined behavior in massive neutron stars, *Nat. Commun.* 14 (2023) 8451. [arXiv:2303.11356](#), [doi:10.1038/s41467-023-44051-y](#).
- [21] E. V. Chimanski, R. V. Lobato, A. R. Goncalves, C. A. Bertulani, Bayesian Exploration of Phenomenological EoS of Neutron/Hybrid Stars with Recent Observations, *Parti.* 6 (2023) 198–216. [arXiv:2205.01174](#), [doi:10.3390/particles6010011](#).
- [22] N. Rutherford, M. Mendes, I. Svensson, et al., Constraining the Dense Matter Equation of State with New *NICER* Mass–Radius Measurements and New Chiral Effective Field Theory Inputs, *Astrophys. J. Lett.* 971 (2024) L19. [arXiv:2407.06790](#), [doi:10.3847/2041-8213/ad5f02](#).
- [23] C. Mondal, F. Gulminelli, Nucleonic metamodelling in light of multimessenger, *PREX-II*, and *CREX* data, *Phys. Rev. C* 107 (2023) 015801. [arXiv:2209.05177](#), [doi:10.1103/PhysRevC.107.015801](#).
- [24] J. Zhou, J. Xu, P. Papakostas, Bayesian inference of neutron-star observables based on effective nuclear interactions, *Phys. Rev. C* 107 (2023) 055803. [arXiv:2301.07904](#), [doi:10.1103/PhysRevC.107.055803](#).
- [25] M. V. Beznogov, A. R. Raduta, Bayesian Survey of the Dense Matter Equation of State Built upon Skyrme Effective Interactions, *Astrophys. J.* 966 (2024) 216. [arXiv:2308.15351](#), [doi:10.3847/1538-4357/ad2f9b](#).
- [26] M. V. Beznogov, A. R. Raduta, Bayesian inference of the dense matter equation of state built upon extended Skyrme interactions, *Phys. Rev. C* 110 (2024) 035805. [arXiv:2403.19325](#), [doi:10.1103/PhysRevC.110.035805](#).
- [27] C. Y. Tsang, M. B. Tsang, W. G. Lynch, R. Kumar, C. J. Horowitz, Determination of the equation of state from nuclear experiments and neutron star observations, *Nat. Astron.* 8 (2024) 328–336. [arXiv:2310.11588](#), [doi:10.1038/s41550-023-02161-z](#).
- [28] S. Traversi, P. Char, G. Pagliara, Bayesian Inference of Dense Matter Equation of State within Relativistic Mean Field Models using Astrophysical Measurements, *Astrophys. J.* 897 (2020) 165. [arXiv:2002.08951](#), [doi:10.3847/1538-4357/ab99c1](#).
- [29] T. Malik, M. Ferreira, B. K. Agrawal, C. Providência, Relativistic Description of Dense Matter Equation of State and Compatibility with Neutron Star Observables: A Bayesian Approach, *Astrophys. J.* 930 (2022) 17. [arXiv:2201.12552](#), [doi:10.3847/1538-4357/ac5d3c](#).
- [30] X. Sun, Z. Miao, B. Sun, A. Li, Astrophysical Implications on Hyperon Couplings and Hyperon Star Properties with Relativistic Equations of States, *Astrophys. J.* 942 (2023) 55. [arXiv:2205.10631](#), [doi:10.3847/1538-4357/ac9d9a](#).
- [31] Z. Zhu, A. Li, T. Liu, A Bayesian Inference of a Relativistic Mean-field Model of Neutron Star Matter from Observations of *NICER* and GW170817/AT2017gfo, *Astrophys. J.* 943 (2023) 163. [arXiv:2211.02007](#), [doi:10.3847/1538-4357/acac1f](#).
- [32] M. V. Beznogov, A. R. Raduta, Bayesian inference of the dense matter equation of state built upon covariant density functionals, *Phys. Rev. C* 107 (2023) 045803. [arXiv:2212.07168](#), [doi:10.1103/PhysRevC.107.045803](#).
- [33] T. Malik, M. Ferreira, M. B. Albino, C. Providência, Spanning the full range of neutron star properties within a microscopic description, *Phys. Rev. D* 107 (2023) 103018. [arXiv:2301.08169](#), [doi:10.1103/PhysRevD.107.103018](#).
- [34] M. Salinas, J. Piekarewicz, Bayesian refinement of covariant energy density functionals, *Phys. Rev. C* 107 (2023) 045802. [arXiv:2301.09692](#), [doi:10.1103/PhysRevC.107.045802](#).
- [35] C. Huang, G. Raaijmakers, A. L. Watts, L. Tolos, C. Providência, Constraining a relativistic mean field model using neutron star mass–radius measurements I: nucleonic models, *Mon. Not. R. Astron. Soc.* 529 (2024) 4650–4665. [arXiv:2303.17518](#), [doi:10.1093/mnras/stae844](#).
- [36] V. Parmar, V. B. Thapa, A. Kumar, D. Bandyopadhyay, M. Sinha, Bayesian inference of the dense-matter equation of state of neutron stars with antikaon condensation, *Phys. Rev. C* 110 (2024) 045804. [arXiv:2409.19451](#), [doi:10.1103/PhysRevC.110.045804](#).
- [37] S. Typel, H. H. Wolter, Relativistic mean field calculations with density dependent meson nucleon coupling, *Nucl. Phys. A* 656 (1999) 331–364. [doi:10.1016/S0375-9474\(99\)00310-3](#).
- [38] G. A. Lalazissis, T. Niksic, D. Vretenar, P. Ring, New relativistic mean-field interaction with density-dependent meson-nucleon couplings, *Phys. Rev. C* 71 (2005) 024312. [doi:10.1103/PhysRevC.71.024312](#).

Table 4: Key quantities of compact stars from the posterior distributions for the different astrophysical scenarios: radii, tidal deformabilities, central baryonic densities, energy densities, pressures, sound speeds, and trace anomalies for 1.0, 1.4, 2.0 M_{\odot} and the maximum-mass stars. We also list the inferred radius differences between 1.4, 2.0 M_{\odot} and 1.0, 1.4 M_{\odot} stars. The upper and lower values correspond to the 95.4% CI.

Par.	Unit	Baseline	Scenario A	Scenario B	Scenario C	Scenario D	Scenario E	Scenario F
$R_{1.0}$	km	12.53 ^{+0.51} _{-0.57}	12.51 ^{+0.38} _{-0.44}	12.44 ^{+0.38} _{-0.43}	12.57 ^{+0.37} _{-0.41}	12.62 ^{+0.45} _{-0.50}	12.53 ^{+0.44} _{-0.49}	12.69 ^{+0.43} _{-0.47}
$\Lambda_{1.0}$		3287 ⁺⁹⁷⁴ ₋₈₄₄	3233 ⁺⁷⁰⁵ ₋₆₅₅	3114 ⁺⁶⁶⁷ ₋₆₁₉	3340 ⁺⁷¹⁷ ₋₆₃₅	3413 ⁺⁸⁸⁵ ₋₇₇₉	3257 ⁺⁸²⁴ ₋₇₂₇	3554 ⁺⁸⁵⁸ ₋₇₆₄
$\rho_{1.0}$	fm ⁻³	0.330 ^{+0.058} _{-0.050}	0.334 ^{+0.045} _{-0.041}	0.342 ^{+0.044} _{-0.041}	0.327 ^{+0.042} _{-0.040}	0.325 ^{+0.050} _{-0.045}	0.335 ^{+0.049} _{-0.045}	0.316 ^{+0.047} _{-0.040}
$P_{1.0}$	MeV/fm ³	28.91 ^{+7.40} _{-5.61}	29.36 ^{+5.68} _{-4.54}	30.27 ^{+5.69} _{-4.52}	28.57 ^{+5.16} _{-4.34}	28.15 ^{+6.25} _{-4.93}	29.30 ^{+6.24} _{-4.99}	27.19 ^{+5.69} _{-4.43}
$\varepsilon_{1.0}$	MeV/fm ³	328.38 ^{+39.78} _{-51.61}	332.78 ^{+47.33} _{-43.22}	340.87 ^{+45.95} _{-42.40}	325.31 ^{+43.88} _{-41.17}	323.00 ^{+51.72} _{-46.86}	333.20 ^{+50.85} _{-46.71}	313.91 ^{+48.94} _{-41.88}
$c_{s,1.0}^2$		0.269 ^{+0.030} _{-0.042}	0.265 ^{+0.032} _{-0.039}	0.263 ^{+0.033} _{-0.037}	0.269 ^{+0.030} _{-0.041}	0.265 ^{+0.032} _{-0.042}	0.262 ^{+0.034} _{-0.039}	0.269 ^{+0.030} _{-0.044}
$\Delta_{1.0}$		0.245 ^{+0.005} _{-0.006}	0.245 ^{+0.004} _{-0.005}	0.244 ^{+0.004} _{-0.005}	0.245 ^{+0.004} _{-0.004}	0.246 ^{+0.004} _{-0.005}	0.245 ^{+0.004} _{-0.005}	0.247 ^{+0.004} _{-0.005}
$R_{1.4}$	km	12.61 ^{+0.65} _{-0.67}	12.56 ^{+0.51} _{-0.52}	12.47 ^{+0.48} _{-0.50}	12.65 ^{+0.49} _{-0.49}	12.69 ^{+0.59} _{-0.60}	12.57 ^{+0.57} _{-0.57}	12.79 ^{+0.55} _{-0.56}
$\Lambda_{1.4}$		515 ⁺²³⁵ ₋₁₆₇	500 ⁺¹⁷⁸ ₋₁₃₃	472 ⁺¹⁶³ ₋₁₂₁	526 ⁺¹⁸⁰ ₋₁₃₄	535 ⁺²¹⁸ ₋₁₅₇	498 ⁺¹⁹⁸ ₋₁₄₁	571 ⁺²⁰⁷ ₋₁₆₂
$\rho_{1.4}$	fm ⁻³	0.405 ^{+0.087} _{-0.077}	0.412 ^{+0.073} _{-0.067}	0.425 ^{+0.070} _{-0.067}	0.400 ^{+0.071} _{-0.063}	0.399 ^{+0.078} _{-0.071}	0.415 ^{+0.076} _{-0.073}	0.384 ^{+0.078} _{-0.062}
$P_{1.4}$	MeV/fm ³	56.090 ^{+19.278} _{-14.503}	57.537 ^{+15.523} _{-12.683}	60.042 ^{+15.313} _{-12.859}	55.151 ^{+14.406} _{-11.782}	54.680 ^{+16.554} _{-13.209}	57.871 ^{+16.524} _{-13.733}	51.927 ^{+15.549} _{-11.458}
$\varepsilon_{1.4}$	MeV/fm ³	412.39 ^{+95.53} _{-83.02}	420.27 ^{+80.62} _{-73.15}	433.76 ^{+76.56} _{-73.38}	406.96 ^{+78.11} _{-67.94}	405.70 ^{+86.29} _{-76.67}	423.26 ^{+82.78} _{-79.02}	389.96 ^{+85.26} _{-66.82}
$c_{s,1.4}^2$		0.378 ^{+0.028} _{-0.050}	0.375 ^{+0.028} _{-0.048}	0.374 ^{+0.030} _{-0.046}	0.377 ^{+0.026} _{-0.049}	0.373 ^{+0.029} _{-0.050}	0.372 ^{+0.031} _{-0.050}	0.376 ^{+0.026} _{-0.054}
$\Delta_{1.4}$		0.197 ^{+0.010} _{-0.013}	0.197 ^{+0.008} _{-0.010}	0.195 ^{+0.008} _{-0.010}	0.198 ^{+0.008} _{-0.009}	0.199 ^{+0.009} _{-0.011}	0.197 ^{+0.009} _{-0.011}	0.200 ^{+0.008} _{-0.010}
$R_{2.0}$	km	12.31 ^{+1.07} _{-1.24}	12.21 ^{+0.92} _{-1.09}	12.04 ^{+0.91} _{-1.03}	12.38 ^{+0.86} _{-1.05}	12.40 ^{+1.00} _{-1.16}	12.17 ^{+1.01} _{-1.11}	12.60 ^{+0.88} _{-1.14}
$\Lambda_{2.0}$		40.3 ^{+42.6} _{-25.0}	37.6 ^{+33.8} _{-22.0}	33.2 ^{+30.6} _{-19.1}	42.4 ^{+33.9} _{-23.9}	42.42 ^{+40.84} _{-25.42}	36.1 ^{+37.0} _{-21.4}	48.9 ^{+38.6} _{-28.6}
$\rho_{2.0}$	fm ⁻³	0.586 ^{+0.290} _{-0.162}	0.603 ^{+0.272} _{-0.151}	0.636 ^{+0.273} _{-0.162}	0.572 ^{+0.248} _{-0.134}	0.574 ^{+0.273} _{-0.151}	0.616 ^{+0.278} _{-0.167}	0.539 ^{+0.254} _{-0.126}
$P_{2.0}$	MeV/fm ³	167.05 ^{+186.55} _{-70.31}	176.17 ^{+176.25} _{-68.20}	193.66 ^{+185.95} _{-76.50}	160.66 ^{+147.96} _{-58.08}	161.06 ^{+168.01} _{-64.43}	182.01 ^{+185.13} _{-75.67}	144.69 ^{+143.77} _{-51.71}
$\varepsilon_{2.0}$	MeV/fm ³	639.98 ^{+398.34} _{-195.40}	662.57 ^{+376.71} _{-185.61}	704.78 ^{+385.85} _{-201.48}	623.64 ^{+336.38} _{-162.73}	626.21 ^{+371.34} _{-182.44}	679.07 ^{+387.85} _{-206.29}	582.67 ^{+339.60} _{-150.38}
$c_{s,2.0}^2$		0.568 ^{+0.063} _{-0.039}	0.571 ^{+0.054} _{-0.035}	0.577 ^{+0.057} _{-0.036}	0.565 ^{+0.045} _{-0.032}	0.563 ^{+0.054} _{-0.038}	0.570 ^{+0.059} _{-0.039}	0.557 ^{+0.045} _{-0.036}
$\Delta_{2.0}$		0.072 ^{+0.043} _{-0.080}	0.068 ^{+0.040} _{-0.074}	0.059 ^{+0.042} _{-0.074}	0.076 ^{+0.035} _{-0.064}	0.076 ^{+0.040} _{-0.073}	0.065 ^{+0.044} _{-0.076}	0.085 ^{+0.033} _{-0.065}
M_{\max}	M_{\odot}	2.26 ^{+0.28} _{-0.21}	2.24 ^{+0.24} _{-0.19}	2.20 ^{+0.23} _{-0.17}	2.27 ^{+0.23} _{-0.21}	2.27 ^{+0.27} _{-0.22}	2.22 ^{+0.26} _{-0.19}	2.32 ^{+0.24} _{-0.24}
$R_{M_{\max}}$	km	11.20 ^{+1.01} _{-0.76}	11.13 ^{+0.84} _{-0.64}	11.00 ^{+0.80} _{-0.58}	11.26 ^{+0.82} _{-0.67}	11.26 ^{+0.96} _{-0.72}	11.09 ^{+0.91} _{-0.64}	11.44 ^{+0.88} _{-0.78}
$\Lambda_{M_{\max}}$		5.80 ^{+1.86} _{-0.85}	5.91 ^{+1.89} _{-0.88}	6.04 ^{+1.78} _{-0.93}	5.75 ^{+1.92} _{-0.77}	5.83 ^{+2.15} _{-0.88}	6.02 ^{+2.00} _{-0.98}	5.64 ^{+2.18} _{-0.73}
$\rho_{M_{\max}}$	fm ⁻³	0.955 ^{+0.168} _{-0.171}	0.970 ^{+0.149} _{-0.152}	0.996 ^{+0.136} _{-0.152}	0.943 ^{+0.152} _{-0.142}	0.945 ^{+0.162} _{-0.162}	0.979 ^{+0.145} _{-0.166}	0.912 ^{+0.169} _{-0.142}
$P_{M_{\max}}$	MeV/fm ³	571.72 ^{+78.72} _{-76.94}	577.90 ^{+64.32} _{-64.69}	588.95 ^{+62.09} _{-62.70}	567.45 ^{+62.15} _{-62.18}	564.65 ^{+71.03} _{-70.65}	579.05 ^{+67.76} _{-69.17}	551.63 ^{+69.28} _{-63.29}
$\varepsilon_{M_{\max}}$	MeV/fm ³	1245.03 ^{+220.16} _{-225.10}	1265.19 ^{+194.04} _{-200.68}	1298.90 ^{+177.49} _{-199.98}	1230.27 ^{+197.18} _{-187.55}	1232.02 ^{+210.66} _{-213.08}	1277.20 ^{+190.11} _{-218.00}	1189.94 ^{+219.07} _{-188.08}
$c_{s,M_{\max}}^2$		0.734 ^{+0.032} _{-0.053}	0.731 ^{+0.031} _{-0.053}	0.726 ^{+0.032} _{-0.049}	0.736 ^{+0.028} _{-0.055}	0.734 ^{+0.032} _{-0.061}	0.727 ^{+0.035} _{-0.055}	0.741 ^{+0.028} _{-0.063}
$\Delta_{M_{\max}}$		-0.130 ^{+0.042} _{-0.026}	-0.127 ^{+0.041} _{-0.026}	-0.123 ^{+0.038} _{-0.027}	-0.131 ^{+0.043} _{-0.023}	-0.129 ^{+0.047} _{-0.026}	-0.124 ^{+0.042} _{-0.028}	-0.134 ^{+0.049} _{-0.023}
$R_{1.4}-R_{2.0}$	km	0.28 ^{+0.76} _{-0.45}	0.33 ^{+0.76} _{-0.44}	0.41 ^{+0.74} _{-0.46}	0.25 ^{+0.72} _{-0.39}	0.27 ^{+0.77} _{-0.44}	0.37 ^{+0.76} _{-0.48}	0.18 ^{+0.75} _{-0.37}
$R_{1.4}-R_{1.0}$	km	0.08 ^{+0.22} _{-0.22}	0.06 ^{+0.22} _{-0.21}	0.03 ^{+0.21} _{-0.20}	0.09 ^{+0.20} _{-0.22}	0.08 ^{+0.22} _{-0.23}	0.04 ^{+0.22} _{-0.21}	0.12 ^{+0.20} _{-0.24}

- [39] J. J. Li, A. Sedrakian, Constraining compact star properties with nuclear saturation parameters, *Phys. Rev. C* 100 (2019) 015809. [arXiv:1903.06057](#), [doi:10.1103/PhysRevC.100.015809](#).
- [40] J. J. Li, A. Sedrakian, Implications from GW170817 for Δ -isobar Admixed Hypernuclear Compact Stars, *Astrophys. J. Lett.* 874 (2019) L22. [arXiv:1904.02006](#), [doi:10.3847/2041-8213/ab1090](#).
- [41] J. J. Li, A. Sedrakian, New Covariant Density Functionals of Nuclear Matter for Compact Star Simulations, *Astrophys. J.* 957 (2023) 41. [arXiv:2308.14457](#), [doi:10.3847/1538-4357/acfa73](#).
- [42] M. G. Alford, A. Schmitt, K. Rajagopal, T. Schäfer, Color superconductivity in dense quark matter, *Rev. Mod. Phys.* 80 (2008) 1455–1515. [arXiv:0709.4635](#), [doi:10.1103/RevModPhys.80.1455](#).
- [43] A. Sedrakian, Impact of Multiple Phase Transitions in Dense QCD on Compact Stars, *Particles* 6 (2023) 713–730. [arXiv:2306.13884](#), [doi:10.3390/particles6030044](#).
- [44] J. J. Li, W. H. Long, A. Sedrakian, Hypernuclear stars from relativistic Hartree-Fock density functional theory, *Eur. Phys. J. A* 54 (2018) 133. [arXiv:1801.07084](#), [doi:10.1140/epja/i2018-12566-6](#).
- [45] J. J. Li, A. Sedrakian, F. Weber, Universal relations for compact stars with heavy baryons, *Phys. Rev. C* 108 (2023) 025810. [arXiv:2306.14190](#), [doi:10.1103/PhysRevC.108.025810](#).
- [46] T. Gorda, O. Komoltsev, A. Kurkela, Ab-initio QCD Calculations Impact the Inference of the Neutron-star-matter Equation of State, *Astrophys. J.* 950 (2) (2023) 107. [arXiv:2204.11877](#), [doi:10.3847/1538-4357/acce3a](#).
- [47] N. Yao, A. Sorensen, V. Dexheimer, J. Noronha-Hostler, Structure in the speed of sound: From neutron stars to heavy-ion collisions, *Phys. Rev. C* 109 (6) (2024) 065803. [arXiv:2311.18819](#), [doi:10.1103/PhysRevC.109.065803](#).
- [48] K. Hebeler, J. M. Lattimer, C. J. Pethick, A. Schwenk, Equation of state and neutron star properties constrained by nuclear physics and observation, *Astrophys. J.* 773 (2013) 11. [arXiv:1303.4662](#), [doi:10.1088/0004-637X/773/1/11](#).
- [49] T. Salmi, D. Choudhury, Y. Kini, et al., The Radius of the High-mass Pulsar PSR J0740+6620 with 3.6 yr of NICER Data, *Astrophys. J.* 974 (2024) 294. [arXiv:2406.14466](#), [doi:10.3847/1538-4357/ad5f1f](#).
- [50] B. P. Abbott, R. Abbott, T. D. Abbott, et al., GW170817: Observation of Gravitational Waves from a Binary Neutron Star Inspiral, *Phys. Rev. Lett.* 119 (2017) 161101. [arXiv:1710.05832](#), [doi:10.1103/PhysRevLett.119.161101](#).
- [51] B. P. Abbott, R. Abbott, T. D. Abbott, et al., GW190425: Observation of a Compact Binary Coalescence with Total Mass $\sim 3.4 M_{\odot}$, *Astrophys. J. Lett.* 892 (2020) L3. [arXiv:2001.01761](#), [doi:10.3847/2041-8213/ab75f5](#).

Table 5: Parameter values for meson-nucleon couplings and their density dependence of CDFs from the posterior distributions for the different astrophysical scenarios. The upper and lower values correspond to the 68.3% CI. The particle masses adopted are same as those in [38, 41].

Par.	Baseline	Scenario A	Scenario B	Scenario C	Scenario D	Scenario E	Scenario F
g_σ	9.96267 ^{+0.61333} _{-0.53389}	9.92663 ^{+0.62975} _{-0.51179}	9.88753 ^{+0.65166} _{-0.53912}	9.96500 ^{+0.60741} _{-0.49946}	10.00233 ^{+0.61930} _{-0.52274}	9.94190 ^{+0.63445} _{-0.54769}	10.04090 ^{+0.59946} _{-0.48718}
g_ω	12.18257 ^{+0.88983} _{-0.79553}	12.12960 ^{+0.91478} _{-0.76465}	12.06945 ^{+0.95002} _{-0.80571}	12.18376 ^{+0.88206} _{-0.74216}	12.23788 ^{+0.89952} _{-0.77561}	12.14935 ^{+0.92510} _{-0.81874}	12.29409 ^{+0.87200} _{-0.71885}
g_ρ	3.60052 ^{+0.17951} _{-0.20111}	3.61178 ^{+0.17926} _{-0.20432}	3.61896 ^{+0.18320} _{-0.20712}	3.60001 ^{+0.18207} _{-0.20211}	3.61310 ^{+0.18343} _{-0.20781}	3.62498 ^{+0.17850} _{-0.20470}	3.60343 ^{+0.18182} _{-0.20629}
a_σ	1.37785 ^{+0.10933} _{-0.07575}	1.36850 ^{+0.09765} _{-0.06810}	1.36845 ^{+0.08465} _{-0.06421}	1.37376 ^{+0.11451} _{-0.07321}	1.36056 ^{+0.11155} _{-0.07101}	1.35816 ^{+0.09134} _{-0.06621}	1.36740 ^{+0.13345} _{-0.08033}
b_σ	0.57954 ^{+0.99226} _{-0.29598}	0.51077 ^{+0.80903} _{-0.25014}	0.45761 ^{+0.64366} _{-0.20903}	0.59951 ^{+1.01785} _{-0.31428}	0.54283 ^{+0.97983} _{-0.28715}	0.45464 ^{+0.71434} _{-0.21850}	0.65861 ^{+1.30231} _{-0.37666}
c_σ	0.94443 ^{+1.59923} _{-0.46813}	0.83475 ^{+1.28249} _{-0.39577}	0.75779 ^{+1.00423} _{-0.33366}	0.96720 ^{+1.65338} _{-0.49289}	0.87042 ^{+1.57783} _{-0.44473}	0.74575 ^{+1.10643} _{-0.34750}	1.04371 ^{+2.13064} _{-0.58378}
d_σ	0.59409 ^{+0.23209} _{-0.12045}	0.63192 ^{+0.23513} _{-0.10860}	0.66323 ^{+0.22829} _{-0.22328}	0.58706 ^{+0.25126} _{-0.23041}	0.61883 ^{+0.12545} _{-0.24985}	0.66856 ^{+0.10384} _{-0.24434}	0.56513 ^{+0.14757} _{-0.24108}
a_ω	1.39328 ^{+0.09414} _{-1.50296}	1.38285 ^{+0.08885} _{-1.22834}	1.38177 ^{+0.08375} _{-1.01049}	1.38960 ^{+0.09184} _{-1.54412}	1.37577 ^{+0.09186} _{-1.49076}	1.37168 ^{+0.08742} _{-1.08372}	1.38367 ^{+0.09998} _{-1.92297}
b_ω	0.58114 ^{+0.32471} _{-2.35744}	0.50515 ^{+0.26753} _{-1.88498}	0.45610 ^{+0.23265} _{-1.51395}	0.60143 ^{+0.34050} _{-2.45403}	0.54736 ^{+0.31193} _{-2.29319}	0.45308 ^{+0.23701} _{-1.61677}	0.66552 ^{+0.40193} _{-3.12799}
c_ω	0.94128 ^{+2.48712} _{-0.48712}	0.82851 ^{+1.40726} _{-0.40726}	0.75653 ^{+1.35083} _{-0.35083}	0.96860 ^{+0.51318} _{-0.26889}	0.87941 ^{+0.46819} _{-0.28467}	0.74542 ^{+0.36095} _{-0.26241}	1.04460 ^{+0.59588} _{-0.29700}
d_ω	0.59509 ^{+0.26163} _{-0.27720}	0.63430 ^{+0.25525} _{-0.28381}	0.66378 ^{+0.24265} _{-0.28062}	0.58663 ^{+0.26889} _{-0.27456}	0.61566 ^{+0.29152} _{-0.29152}	0.66871 ^{+0.29306} _{-0.29306}	0.56489 ^{+0.28225} _{-0.28225}
a_ρ	0.57179 ^{+0.10605} _{-0.09381}	0.56209 ^{+0.10469} _{-0.08985}	0.55821 ^{+0.10244} _{-0.08862}	0.57125 ^{+0.10743} _{-0.09389}	0.55872 ^{+0.10873} _{-0.09529}	0.55024 ^{+0.10437} _{-0.08917}	0.56482 ^{+0.11375} _{-0.09668}

- [52] G. Raaijmakers, S. K. Greif, K. Hebeler, et al., Constraints on the Dense Matter Equation of State and Neutron Star Properties from NICER's Mass-Radius Estimate of PSR J0740+6620 and Multimessenger Observations, *Astrophys. J. Lett.* 918 (2021) L29. [arXiv:2105.06981](#), [doi:10.3847/2041-8213/ac089a](#).
- [53] F. Hernandez Vivanco, R. Smith, E. Thrane, P. D. Lasky, A scalable random forest regressor for combining neutron-star equation of state measurements: A case study with GW170817 and GW190425, *Mon. Not. R. Astron. Soc.* 499 (2020) 5972–5977. [arXiv:2008.05627](#), [doi:10.1093/mnras/staa3243](#).
- [54] J. Antoniadis, P. C. C. Freire, N. Wex, et al., A Massive Pulsar in a Compact Relativistic Binary, *Science* 340 (2013) 6131. [arXiv:1304.6875](#), [doi:10.1126/science.1233232](#).
- [55] H. T. Cromartie, E. Fonseca, S. M. Ransom, et al., Relativistic Shapiro delay measurements of an extremely massive millisecond pulsar, *Nat. Astron.* 4 (2019) 72–76. [arXiv:1904.06759](#), [doi:10.1038/s41550-019-0880-2](#).
- [56] E. Fonseca, H. T. Cromartie, T. T. Pennucci, et al., Refined Mass and Geometric Measurements of the High-mass PSR J0740+6620, *Astrophys. J. Lett.* 915 (2021) L12. [arXiv:2104.00880](#), [doi:10.3847/2041-8213/ac03b8](#).
- [57] R. Abbott, T. D. Abbott, S. Abraham, et al., GW190814: Gravitational Waves from the Coalescence of a 23 Solar Mass Black Hole with a 2.6 Solar Mass Compact Object, *Astrophys. J. Lett.* 896 (2020) L44. [arXiv:2006.12611](#), [doi:10.3847/2041-8213/ab960f](#).
- [58] Y. Fujimoto, K. Fukushima, L. D. McLerran, M. Praszalowicz, Trace Anomaly as Signature of Conformality in Neutron Stars, *Phys. Rev. Lett.* 129 (25) (2022) 252702. [arXiv:2207.06753](#), [doi:10.1103/PhysRevLett.129.252702](#).
- [59] C. Musolino, C. Ecker, L. Rezzolla, On the Maximum Mass and Oblateness of Rotating Neutron Stars with Generic Equations of State, *Astrophys. J.* 962 (2024) 61. [arXiv:2307.03225](#), [doi:10.3847/1538-4357/ad1758](#).
- [60] N. Yao, A. Sorensen, V. Dexheimer, J. Noronha-Hostler, Structure in the speed of sound: From neutron stars to heavy-ion collisions, *Phys. Rev. C* 109 (2024) 065803. [arXiv:2311.18819](#), [doi:10.1103/PhysRevC.109.065803](#).
- [61] Y. Fujimoto, K. Fukushima, K. Murase, Mapping neutron star data to the equation of state using the deep neural network, *Phys. Rev. D* 101 (2020) 054016. [arXiv:1903.03400](#), [doi:10.1103/PhysRevD.101.054016](#).
- [62] I. Tews, J. Carlson, S. Gandolfi, S. Reddy, Constraining the speed of sound inside neutron stars with chiral effective field theory interactions and observations, *Astrophys. J.* 860 (2018) 149. [arXiv:1801.01923](#), [doi:10.3847/1538-4357/aac267](#).
- [63] P. Bedaque, A. W. Steiner, Sound velocity bound and neutron stars, *Phys. Rev. Lett.* 114 (2015) 031103. [arXiv:1408.5116](#), [doi:10.1103/PhysRevLett.114.031103](#).
- [64] O. Komoltsev, R. Somasundaram, T. Gorda, A. Kurkela, J. Margueron, I. Tews, Equation of state at neutron-star densities and beyond from perturbative QCD, *Phys. Rev. D* 109 (9) (2024) 094030. [arXiv:2312.14127](#), [doi:10.1103/PhysRevD.109.094030](#).
- [65] D. Klahn, T. Blaschke, S. Typel, et al., Constraints on the high-density nuclear equation of state from the phenomenology of compact stars and heavy-ion collisions, *Phys. Rev. C* 74 (2006) 035802. [arXiv:nucl-th/0602038](#), [doi:10.1103/PhysRevC.74.035802](#).
- [66] A. Sedrakian, Short-Range Correlations and Urca Process in Neutron Stars, *Phys. Rev. Lett.* 133 (2024) 171401. [arXiv:2406.16183](#), [doi:10.1103/PhysRevLett.133.171401](#).